Crystallization of amorphous GeTe simulated by neural network potential addressing medium-range order

Dongheon Lee[1], Kyeongpung Lee[1], Dongsun Yoo, Wonseok Jeong, Seungwu Han[*]

Department of Materials Science and Engineering, Seoul National University, Seoul 08826, Republic of Korea

ABSTRACT

For the last decade, crystallization kinetics of phase change materials has been intensively investigated by molecular dynamics simulations. In particular, recent machine-learning potentials have advanced microscopic understanding of crystallization behavior of phase change materials by overcoming the computational limit of the density functional theory (DFT). Here we develop neural network potentials (NNP) for GeTe, an archetypal phase change material, and study the crystallization of amorphous GeTe. Consistently with the previous literature, we find that NNP results in a very short incubation time and the crystallization completes within a few nanoseconds, which is at variance with experimental measurement as well as DFT simulations. We show that such deficiencies of NNP originate from overly flat fourfold rings in the amorphous structure. By including explicitly relaxation paths from flat to puckered fourfold rings, we generate a modified NNP, which produces medium-range orders that are more consistent with DFT. Using the modified NNP, crystallization simulations are performed at two densities that represent partially or fully amorphized devices, and temperatures ranging from 500 to 650 K. At both densities, finite incubation times are clearly observed. In particular, the incubation time under the partially amorphized device condition is found to be 7 or 17 ns, which is consistent with experiments. By proposing a method to develop NNPs with correct medium-range order, this work will contribute to simulating phase change materials more accurately and realistically.

1. Introduction

Phase-change materials display distinct optical and electrical properties between crystalline and amorphous phases, which enables applications to electronic and optical memory devices. In particular, the phase-change memory (PCM) employing GeTe-Sb$_2$Te$_3$ (GST) pseudo-binary compounds benefits from rapid phase-switching [1], low power consumption [2], high thermal stability [3], and long cyclability [4], thus attracting wide interests as a next-generation memory device. Recently, a new type of memory architecture based on PCM was commercialized [5–7], which makes potential use for faster storage or near-memory application in data centers or workstations [8]. In addition, variable resistance states in PCM is advantageous for neuromorphic computing [9].

The crystallization behavior, especially crystallization speed, of GST is a critical material parameter in PCM applications. For example, if PCM can operate with a crystallization speed of sub 10 ns, it can directly compete with conventional memories such as dynamic random-access memory (DRAM). As such, the crystallization kinetics of GST has

been a subject of intensive studies in both experiment and theory. On the theoretical side, the fast phase-switching of GST allows for direct simulations of crystallization of the amorphous phase using *ab initio* molecular dynamics (AIMD) based on the density functional theory (DFT), enlightening crystallization mechanism at the atomic scale. For example, it was found that fast crystallization of GST originates from the medium-range order represented by fourfold rings [10]. The AIMD simulation can also reveal the effect of dopants explicitly; it was demonstrated that Bi dopants shorten the crystallization time, but N dopants hinder growth of crystal planes by distorting fourfold rings [11,12]. However, since AIMD is limited to model systems with a few hundreds of atoms, the computational results on disordered phases are significantly influenced by finite-size effects.

Recently, machine-learning approaches are attracting wide interests as they are poised to overcome the computational limitation of AIMD [13]. In this method, general mathematical models such as neural network [14] and Gaussian process [15] are trained over *ab initio* energies and predict energies of untrained structures with computational speeds higher than *ab initio* methods by thousands-fold. The machine-

---

learning approach to construct the classical potential is particularly useful for systems with complicated bonding natures such as GST. In Refs. [16–22], the neural network potential (NNP) was developed for amorphous GeTe (*a*-GeTe) and employed in a variety of simulations that go far beyond the current scope of AIMD. In particular, the crystallization behavior of *a*-GeTe models with a realistic scale was extensively studied, analyzing influences of temperature and interface [17,18].

In the previous simulation of GeTe using the machine-learning potential [17], we pay attention to one critical aspect in the simulation results: the crystallization showed very short incubation periods (the time span before appearance of supercritical nuclei [23]) at most temperatures between 500 and 650 K. This contrasts with many AIMDs on GeTe and Ge$_2$Sb$_2$Te$_5$ that record salient incubation periods of 0.1 ~ 2 ns [10–12,23–28]. Such incubation-free growths are reminiscent of the crystallization behavior of Ge$_2$Sb$_2$Te$_5$ with a pre-existing crystalline seed [29], implying that NNP may have underestimated the nucleation barrier. Furthermore, in Ref. [17], the entire crystallization process including nucleation and growth completes within a few nanoseconds over temperatures between 500 and 650 K, at variance with experiments reporting the minimum crystallization time of ~30 ns for laser-induced crystallization for melt-quenched GeTe samples [30,31]. The electrical-pulse experiment on PCM employing Ge$_2$Sb$_2$Te$_5$ also found that the phase change takes at least 10 ns. [2,32–34] Since the maximum crystal growth velocity in Ref. [17] is only about a factor of 2 higher than the experimental value [35], this indicates that the nucleation rate might be overestimated in the simulation. We note that crystallization time of only 1 ns was reported for PCM with 20-nm thick GeTe [36]. In this case, the crystalline rim surrounding amorphous region lead to a growth-dominated crystallization, skipping the nucleation stage.

In this work, to address and resolve the above issue, we closely analyze the amorphous GeTe obtained through melt-quench simulation with NNP. We find that the degree of planarity of fourfold rings, which represents the medium-range order, is overestimated by NNP, resulting in a low nucleation barrier. By including relaxation trajectories by DFT into the training set, we find significant improvements in the fine feature of medium-range order. The improved NNP allows for studying crystallization more realistically. The remaining sections are organized as follows: we discuss details on training NNP and simulation setup in Section 2. In Section 3.1, we reproduce the abnormally fast crystallization of conventional NNP and suggest an approach to improve NNP. In the ensuing Sections of 3.2 and 3.3, we analyze the structural property and crystallization behavior by the improved NNP, respectively. Section 4 summarizes this work.

2. Methods

2.1. Training NNP

We train NNP over reference structures made of various liquid, amorphous, and crystalline phases, as summarized in Table 1. (Full details of the training set are provided in the Supplementary information.) These structures are mostly sampled from trajectories during AIMD carried out with Vienna *Ab initio* Simulation Package (VASP) [37,38]. The Perdew-Burke-Ernzerhof functional is employed to approximate exchange–correlation energies of electrons [39] and the energy cutoff for the plane-wave basis is set to 200 eV during AIMD. The total energies and atomic forces for reference structures are recalculated with higher accuracy by adopting the energy cutoff of 400 eV and a k-point grid with spacing smaller than 0.314 Å^{-1}. These settings ensure convergence of total energies and atomic forces to within 1 meV/atom and 0.05 eV/Å, respectively.

In Table 1, besides standard structures with stoichiometric GeTe, we include MD trajectories produced in certain processes to enhance accuracy and stability of NNP. For instance, the melting process of crystal

includes information on the energy barrier between liquid and crystal, which is found to be effective in preventing facile crystallization during melt-quench processes. On the other hand, the structures sampled from unary Ge and Te liquids and their diffusional mixing are employed to rectify ad hoc energy mapping in multi-component systems [40], precluding phase separation during liquid simulations. The "ring relaxation" structure in Table 1 will be explained in Section 3.1. In Table 1, root-mean-square errors (RMSE) for energy is the largest for the amorphous structure. However, variations in RMSE by a few meV/atom can result from different distributions of initial weights, and NNPs from independent trainings produce the maximum error for other structural subsets. (See the Supplementary information for details.) This reflects a stochastic nature of learning procedure.

We train NNP using SIMPLE-NN [41]. The structure of the neural network is 70-30-30-1 with atom-centered symmetry functions as input features that encode the local environment around an atom [42]. The symmetry functions consisting of 16 radial and 54 angular components are evaluated with a cutoff radius of 7 Å. Specific parameters for each symmetry function are the same as in Ref. [43]. Since the symmetry functions are highly correlated with each other, decorrelating them with principal component analysis (PCA) accelerates convergence in training. Thus, we transform symmetry function vectors by PCA without truncating dimensions. After the transformation, variances of all components are further normalized (whitened). The loss function is defined as the sum of RMSE for energy and force and L2 regularization term with a coefficient of 10^{-8}. The regularization term is used and its optimized coefficient is determined to prevent undertraining or overfitting of the ring relaxation data. (See the Supplementary information for the detailed procedure.) One-fifth of the training data are randomly chosen and used as a validation set.

In the present work, we develop two types of NNP. The first one, named c-NNP, is constructed in a conventional way by including the reference structures in Table 1 except for the "ring relaxation." As we will discuss in the next section in more detail, c-NNP is equivalent to that used in the previous literatures, describing the medium-range order inaccurately by flattening fourfold rings. To improve this, we add to the training set trajectories followed when *a*-GeTe obtained with c-NNP is relaxed under DFT. For convenience, we call this updated NNP as m-NNP. The RMSEs for energy and force of the validation set are shown in Table 1. The total RMSEs for energy and force are under 5.0 meV/atom and 0.3 eV/Å, respectively. See the Supplementary information for further details of training quality.

2.2. Classical molecular dynamics simulations

All the classical MD simulations based on NNP are performed by the LAMMPS package [44]. The amorphous model of 4096-atom GeTe is generated by the melt-quench process. The initial 4096-atom liquid model (*l*-GeTe) with the cubic cell is set by replicating a snapshot from 64-atom AIMD trajectories at 1000 K. The initial structure is equilibrated for 100 ps at 1000 K and quenched to 300 K with a acooling rate of − 15 K/ps [45]. During the whole melt-quench process, the density is fixed to 34.6 atoms/nm^3 that corresponds to an experimental density of *a*-GeTe [46]. Finally, the cell volume and atomic coordinates of the quenched structure are relaxed at 0 K. The temperature is controlled by the Nosé-Hoover thermostat and a time step of 1 fs is used. The structural features of *l*-GeTe and *a*-GeTe such as the radial distribution function (RDF) and the angular distribution function (ADF) are obtained by averaging over MD trajectories at 1000 and 300 K, respectively.

To investigate the crystallization kinetics of *a*-GeTe, we perform NVT simulations with temperatures ranging from 500, 550, 600 and 650 K. These temperatures are between the melting point (998 K) and the glass-transition temperature (445 K) of GeTe [47,48]. It is known that the density critically affects the crystallization speed of GST [26]. In PCM devices, GeTe is partly amorphized in the rigid cell that

Table 1

Summary of reference structures and root-mean-square errors (RMSEs) for the validation set. The first column describes the structure type of training data. The second and third columns are the number of structures and total atoms (training points) corresponding to the specific structure type, respectively. The fourth and fifth columns show RMSEs for the energy and force, respectively.

Structure type	Number of structures	Number of training points	RMSE$_{energy}$ (meV/atom)		RMSE$_{force}$ (eV/Å)	
			c-NNP	m-NNP	c-NNP	m-NNP
Crystal	504	28,471	3.14	2.48	0.16	0.17
Liquid	500	48,000	4.41	4.05	0.26	0.28
Amorphous	251	24,096	7.24	6.20	0.26	0.28
Quenching (1000 → 300 K)	518	49,728	5.81	3.67	0.25	0.27
Melting (FCC → liquid)	352	33,792	5.11	3.47	0.23	0.26
Mixing liquid (Ge + Te)	301	57,920	3.75	3.07	0.26	0.30
Liquid (Ge or Te)	375	37,500	3.92	3.48	0.26	0.27
Ring relaxation (NNP → DFT)	774	74,304		3.54		0.16
Total	3,575	347,711	4.99	3.65	0.24	0.25

maintains the crystalline volume and so the material is under a high pressure [49]. We consider this by setting the density during crystallization to a value between crystalline and amorphous densities. (See the next section for specific values.) The crystallization behavior is monitored by employing order parameters (Q_8 and Q_{12}) suggested in Ref. [50]. The order parameters are evaluated by considering neighboring atoms within 6 Å and the atom is labelled as crystalline when Q_8 and Q_{12} values are larger than 0.21 and simultaneously, it has three such atoms within 3.2 Å. We calculate the growth speed of crystals from the time derivative of the radius of the hypothetical crystal sphere whose volume corresponds to the sum of the volume of crystalline atoms [17]. (When there are multiple nuclei, each nucleus is monitored separately in evaluating the growth speed.)

3. Results and discussion

3.1. Crystallization of a-GeTe by c-NNP

The amorphous structure of GeTe is first obtained by c-NNP following the melt-quench process explained above. After melt-quench process, the optimized density of a-GeTe by c-NNP is 31.2 atoms/nm^3 which is favorably compared with DFT value (31.9 atoms/nm^3). For comparison, the density of fcc GeTe is 36.6 and 36.9 atoms/nm^3 with c-NNP and DFT, respectively. The structural properties of liquid and amorphous GeTe are in reasonable agreement with DFT as well as the previous NNP result [16]. (See the Supplementary information for details.) Assuming that about 10% of the cell volume transformed into a-GeTe, we set the density for the crystallization simulation to 33.2 atoms/nm^3 [49]. (To note, 33.5 atoms/nm^3 was used in Refs. [17,22].)

The computational results on the crystallization of a-GeTe are shown in Fig. 1. The growth of crystalline nuclei is similar to Ref. [17] and reproduces issues mentioned in the introduction. To iterate, the crystallization completes too fast within a few nanoseconds and the incubation period is very short except for 650 K. The growth speed of crystalline GeTe is computed to be 1.89, 2.71, 4.58, and 6.63 m/s at 500, 550, 600, and 650 K, respectively. These results compare reasonably with the Ref. [17] reporting corresponding values of 0.52, 1.93, 3.60, and 5.09 m/s. Experimentally, the ultrafast differential scanning calorimetry (DSC) measured corresponding growth speeds as 0.0001, 0.05, 0.51, and 1.53 m/s, respectively [35].

To reveal the origin of fast crystallization, we examine the structural properties of a-GeTe generated by c-NNP. As shown in the Supplementary information (and also Fig. 3), RDF indicates that the short-range order agrees well with DFT but the second peak is sharper, implying that the medium-range order may deviate from that of DFT. In addition, ADF around 90° is also more pronounced than in DFT. Since the medium-range order in a-GeTe is characterized by the fourfold rings, we closely examine the geometry of these rings. In particular, we
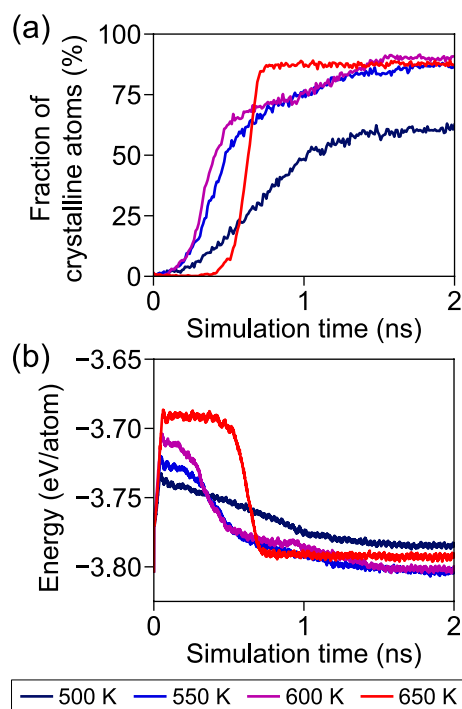

Fig. 1. Time evolution of (a) the percentage of crystalline atoms and (b) potential energy during the crystallization at different temperatures using c-NNP. The simulations are performed with a density corresponding to the device condition.

note that the shape of the fourfold ring is perfectly planar in fcc GeTe but puckered in a-GeTe. As a quantitative metric of the structural deformation, we calculate the inter-diagonal distance (d) in a folded fourfold ring (see inset of Fig. 2 (a)). The d value is zero for the perfectly flat ring (as in fcc GeTe) and increases with the degree of non-planarity. Fig. 2(a) shows the distribution of d that is obtained by MD simulations at 300 K. It is seen that c-NNP produces a distribution that is significantly biased toward zero in comparison with DFT. (The average values are 0.41 and 0.55 Å for c-NNP and DFT, respectively.) More planar fourfold rings in c-NNP are consistent with ADF that is sharper around 90° compared to DFT (see above). Since fcc GeTe consists of only flat fourfold rings, these observations indicate that the geometry of fourfold rings in a-GeTe from c-NNP is closer to the structural motif in the crystalline GeTe than those from DFT.

The classical nucleation theory [51] can relate the structural feature in Fig. 2(a) to the facile nucleation. In this theory, the Gibbs free energy change (ΔG) for a crystalline nucleus with the radius r is defined as
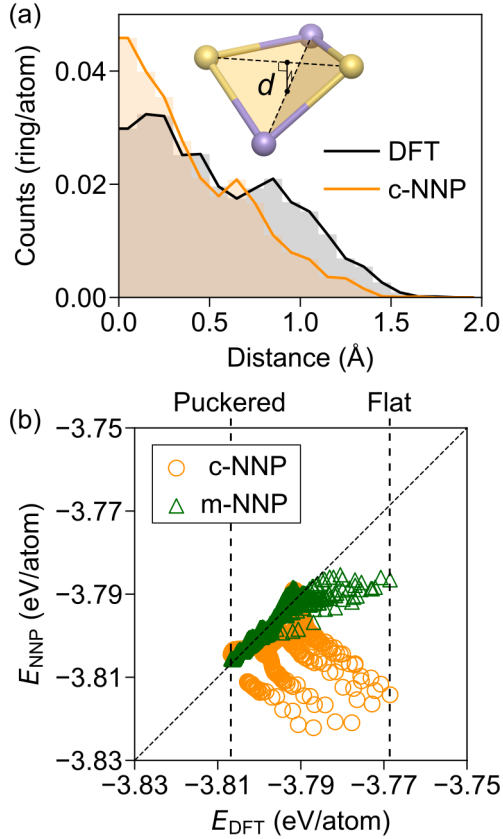
Fig. 2. (a) Planarity: histogram of inter-diagonal distances of fourfold rings (see inset) in *a*-GeTe obtained by DFT and c-NNP. The histogram is obtained by sampling 500 snapshots of 96-atom MD simulations at 300 K. The distance characterizes flatness of the fourfold ring; $d = 0$ indicates that the four atoms forming the ring lie in one plane while d increases as the ring is folded. (b) The energy correlation between DFT and NNP for five DFT-relaxed trajectories of *a*-GeTe generated by c-NNP. High-energy structures (marked as 'Flat') in DFT contain fourfold rings with small d values that increase as the structure relaxes to low-energy one (marked as 'Puckered').

$$\Delta G(r) = -\Delta G_{ac} \frac{4}{3} \pi r^3 + \sigma_{ac} 4 \pi r^2 \qquad (1)$$

where ΔG_{ac} and σ_{ac} are the Gibbs free energy difference and the interfacial free energy between the amorphous and crystalline phases. The critical radius (r_c) that splits decay and growth of the nucleus is given by $\Delta G'(r_c) = 0$:

$$r_c = 2\sigma_{ac}/\Delta G_{ac} \qquad (2)$$

The nucleation barrier (ΔG_c) is equal to $\Delta G(r_c)$:

$$\Delta G_c = \frac{16}{3} \frac{\sigma_{ac}^3}{(\Delta G_{ac})^2} \qquad (3)$$

The similarities in the medium-range order between amorphous and crystalline GeTe in Fig. 2(a) means that σ_{ac} within c-NNP is smaller than for DFT. Since the internal energy difference is similar between c-NNP and DFT (97 versus 99 meV/atom), Eqs. (2) and (3) indicate that r_c and ΔG_c might be small with c-NNP, accounting for the facile nucleation found in Fig. 1.

To improve accuracy in the medium-range order, i.e., the planarity of fourfold rings, we attempted various approaches such as employing symmetry functions with a fine resolution in angles, increasing the cutoff radii of symmetry functions, additional training data on the amorphous structure or crystallization trajectories within DFT, and weighting scheme to compensate for sampling biases [52]. Among them, we find that the most effective one is to add the relaxation

trajectories under DFT to the training set. In detail, we generate five 96-atom models of *a*-GeTe using c-NNP and relax them within DFT. As the structure relaxes, the distribution of d shifts from c-NNP to DFT in Fig. 2(a). Fig. 2(b) shows the energy correlation between DFT and c-NNP along the relaxation paths and it is seen that the stable amorphous structures in c-NNP are unstable in DFT and vice versa, consistent with the structural discrepancy. By including these trajectories into the training set, we construct a modified potential (m-NNP). Table 1 confirms that the overall training accuracy of m-NNP is on par with that of c-NNP. In Fig. 2(b), it is seen that the energy correlation with DFT is significantly improved by m-NNP. In the next subsection, we will discuss the structural properties of *a*-GeTe generated by m-NNP including the planarity of fourfold rings.

3.2. Structural properties of a-GeTe generated by m-NNP

Using m-NNP developed in the above, we obtain *a*-GeTe following the melt-quench process described in Section 2.2. The average density of relaxed structures is 31.9 atoms/nm³, matching to that of DFT (31.9 atoms/nm³). The energy difference between an amorphous structure and fcc crystal is 99 and 90 meV/atom in DFT and m-NNP, respectively. The structural properties of *l*-GeTe and *a*-GeTe are presented in Fig. 3 and compared among DFT, c-NNP, and m-NNP. Fig. 3(a) and 3(b) show RDF and ADF of *l*-GeTe at 1000 K, respectively. It is seen that the liquid structure by m-NNP - is in good agreement with that by DFT, closely reproducing peak positions, heights, and widths. In particular, both DFT and m-NNP produce a main peak around 90° and a shoulder peak around 60°.

Fig. 3(c) and 3(d) show total RDF and ADF of the *a*-GeTe at 300 K and Fig. 3(e)-(g) show partial RDFs of *a*-GeTe at 300 K. The coordination numbers, computed by integrating RDF within 3.2 Å, are 3.94, 3.94, and 3.97 for Ge and 3.09, 3.02, and 3.10 for Te in DFT, m-NNP, and c-NNP, respectively. Compared to c-NNP, the first peak of Ge-Ge and the second peak of Te-Te bond are improved by m-NNP; the first peak position of Ge-Ge is 2.67 Å (2.72 Å in c-NNP), which is close to 2.65 Å in DFT. While the position of the second peak of Te-Te is similar between DFT (4.15 Å), m-NNP (4.09 Å), and c-NNP (4.13 Å), the height of the second peak (2.60 in DFT) is improved in m-NNP (2.72), compared to c-NNP (3.08). However, it is found that the sharpened second peak in RDF and the overestimated peak around 90° in ADF still remain. In our opinion, the fine details of the medium-range order are difficult to fully reproduce with the machine-learning potential because input features or symmetry functions primarily focus on the short-range order.

We further analyze the medium-range order by ring analysis. The number of primitive rings is computed by R.I.N.G.S. code [53] and ring distributions are shown in Fig. 3(h). The overall ring distribution of m-NNP is close to that of DFT. In particular, the fraction of ABAB-type (A = Ge and B = Te) within fourfold rings is about 80% for m-NNP and DFT (see hatched regions). In c-NNP, this fraction is 86%, slightly overestimated. Fig. 3(i) shows distributions of the inter-diagonal distance in fourfold rings. The average value of d is 0.43 Å for m-NNP, showing that the distribution shifts away from zero compared to c-NNP. Although highly distorted fourfold rings ($d < 0.50$ Å) are still suppressed than in DFT, the number of the planar fourfold rings ($d < 0.25$ Å) is almost the same as that of DFT. (The corresponding distributions at 500 K and various density conditions are presented in the Supplementary information and they are consistent with Fig. 3(i).) We also calculate interfacial energies between crystal and amorphous phases (σ_{ac} in Eq. (1)) by following the method in Ref. [54]. The interfacial energies are 0.062 and 0.075 J/m² in c-NNP and m-NNP, respectively. (For comparison, σ_{ac} of GST was experimentally estimated to be 0.075 J/m² by fitting to an expression by Spaepen and Meyer. [55,56].) Combined with Eq. (3), this indicates that m-NNP may have larger nucleation barriers than c-NNP. Therefore, it is expected that the issue of fast crystallization would be resolved by m-NNP as medium-
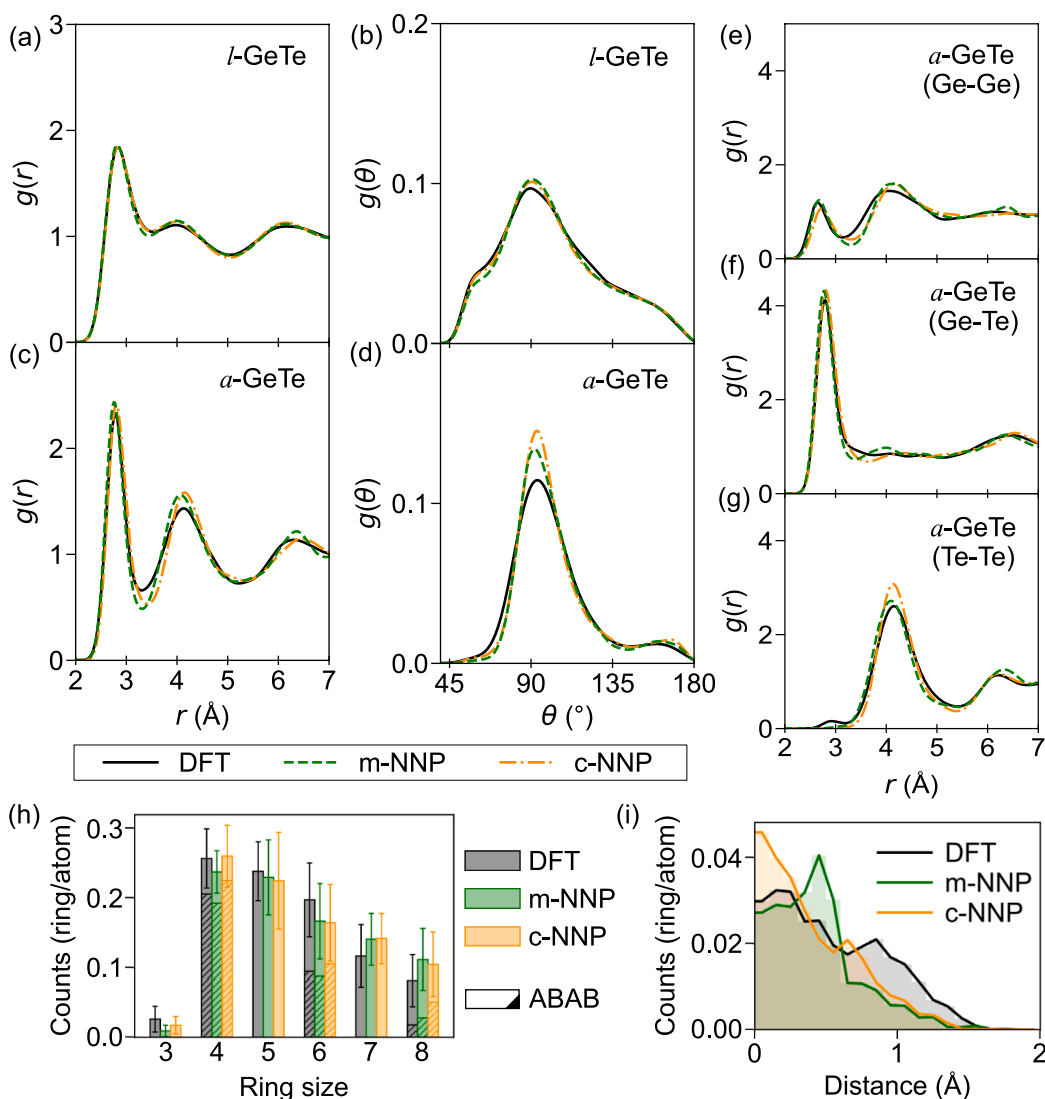
Fig. 3. Structural properties of liquid and amorphous phases of GeTe. (a) RDF and (b) ADF of liquid GeTe at 1000 K. (c) RDF and (d) ADF of *a*-GeTe. (e-g) Partial RDFs of (e) Ge-Ge, (f) Ge-Te, and (g) Te-Te of *a*-GeTe at 300 K. (h) Ring statistics of *a*-GeTe at 300 K. Error bars indicate one standard deviation. The ABAB-type rings (A = Ge and B = Te) for even-membered rings are also shown. (i) Planarity of fourfold rings in *a*-GeTe at 300 K by DFT and m-NNP obtained by the same method as in Fig. 2(a). ADFs and ring statistics are computed with the bonding cutoff of 3.2 Å. The black, green, and orange lines represent the results of DFT, m-NNP, and c-NNP, respectively.

range as well as short-range orders are captured properly. The results for crystallization simulations using m-NNP will be presented in the next section.

3.3. Crystallization simulations using m-NNP

In Fig. 4(a) and 4(b), we carry out the crystallization simulation using m-NNP with the density fixed to 33.7 atoms/nm^3 that considers a device condition. (There are two runs at 500 K.) In comparison with Fig. 1, qualitative differences are noticeable. First, within 20 ns, the crystallization is completed only at 500 K. The incubation period, in this case, is as long as 7 or 17 ns, a time scale comparable to the experiments [30,31]. (The large difference between two runs reflects stochastic nature of nucleation and finite-size effects of the present simulation cell.) This is in contrast with Fig. 1 and Ref. [17] in which at 500 K, the crystallization starts immediately after the simulation begins. This indicates that the crystallization of *a*-GeTe at this condition is nucleation-limited, rather than growth-limited. At higher temperatures, the nucleation is retarded because ΔG_{ac} is reduced and therefore, the nucleation barrier increases following Eq. (3).

Fig. 5 displays the snapshots of a crystalline nucleus growing at 500 K taken at circled instances in Fig. 4(a), and it is seen that a single crystalline grain grows almost isotropically. The growth speeds are 1.31 and 3.82 m/s for the two runs, respectively, which are similar to 1.89 m/s for c-NNP in Fig. 1(a). We also estimate growth speeds at

550–650 K by taking snapshots from 500 K simulation including a supercritical nucleus and annealing them at the elevated temperatures, since supercritical nucleus is not observed at these temperatures during the present simulation time. The calculated growth speeds are 2.58, 3.77, and 3.86 m/s at 550, 600, and 650 K respectively, which agrees reasonably with Ref. [17] (1.88, 3.60, and 5.12 m/s, respectively) as well as results by c-NNP (see above). After the crystallization completes, we analyze the defects within the crystalline grain and find that the defect density is 5% and antisite defects Ge$_{Te}$, and consequently Ge-Ge homopolar bonds, are the most frequent. As a result, the composition of the crystalline region becomes Ge$_{51}$Te$_{49}$ which is slightly Ge-rich. This is in a good agreement with the spectroscopic measurement that estimates 10% of Ge-Ge bonds and Ge vacancies in crystallized GeTe films [57].

We further study the influence of pressure on the crystallization behavior by carrying out another set of simulations at the crystalline density (36.1 atoms/nm^3). This condition would correspond to the case wherein the whole region of the PCM cell is amorphized. (In experiment, PCM cells are fabricated and confined with phase-change materials in crystalline states.) As shown in Fig. 4(c) and 4(d), the crystallization is completed within 4 ns at all the temperatures, much faster than Fig. 4(a) and 4(b). This is mainly because the incubation time is decreased substantially; as the pressure is increased, we find that the population of planar fourfold rings also increases (see the Supplementary information), which may lower the nucleation barrier
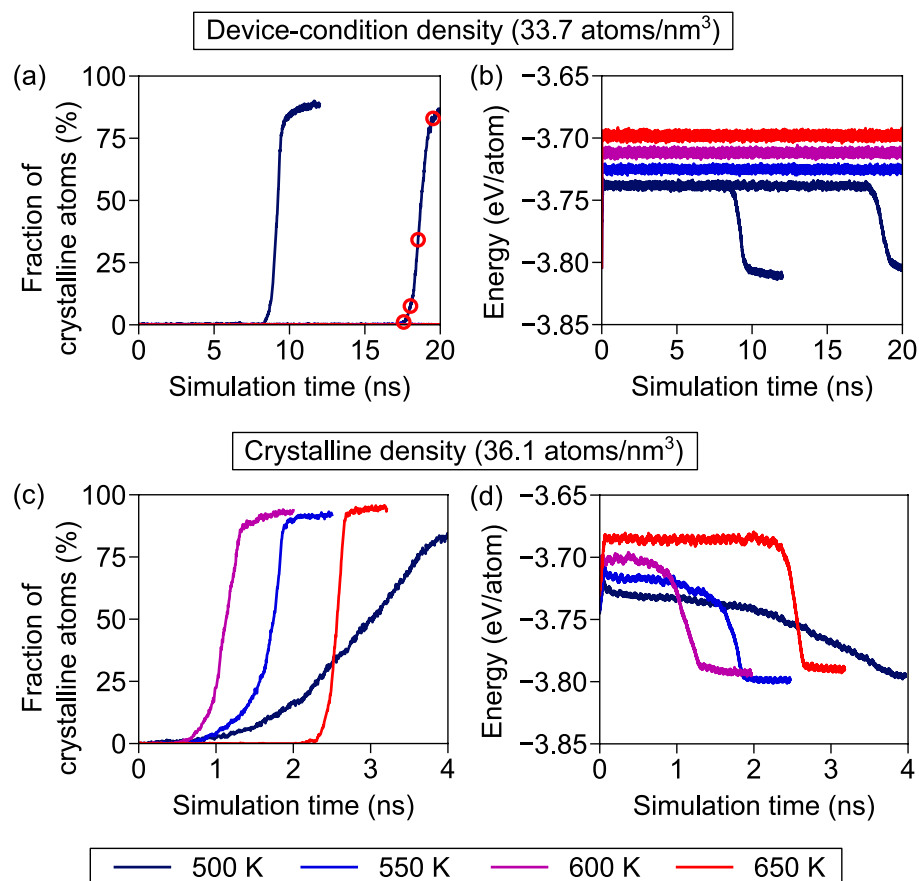
Fig. 4. Time evolution of the percentage of crystalline atoms in 4096-atom cells and the potential energy during the crystallization at 500, 550, 600, and 650 K (a,b) with the density corresponding to the device condition (33.7 atoms/nm³) and (c,d) under the crystalline density (36.1 atoms/nm³). The snapshots at the circled instances in (a) are presented in Fig. 5.
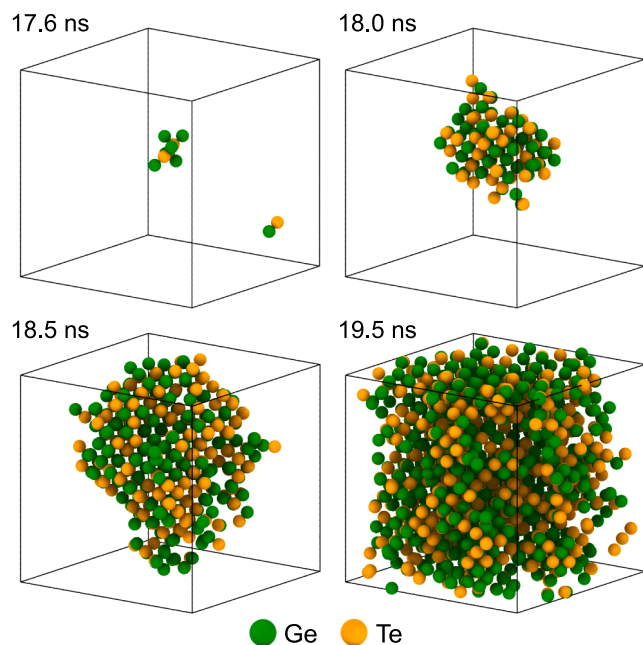

Fig. 5. Crystal growth of GeTe inside the amorphous phase. Only atoms that have crystalline order parameters (see the main text) are visualized. Four snapshots are selected along the crystallization simulation at 500 K under the density corresponding to the device condition (marked as red circles in Fig. 4(a)).

by reducing σ_{ac}. Nevertheless, Fig. 4(c) clearly shows the presence of incubation time at all temperatures. At 500 K, we observe multiple nucleation sites (four), implying that the nucleation is facile. The crystalline growth speed at this temperature is 0.5 m/s, substantially smaller than at the device condition. This is because atomic migration is suppressed at higher densities.

4. Summary

In summary, we developed NNPs to investigate the atomic-scale crystallization behavior of GeTe. It was found that NNP constructed in the conventional way reproduced satisfactorily the overall structural properties of liquid and amorphous GeTe at the DFT level. However, overly flat fourfold rings significantly shortened the incubation time, which is not compatible with experiments and *ab initio* simulations. By including the relaxation path from flat to puckered fourfold rings explicitly, we were able to generate an improved NNP that produces medium-range orders that are more consistent with DFT. Using the modified NNP, crystallization simulations were performed at two densities representing partially and fully amorphized devices, and temperatures ranging from 500 to 650 K. At both densities, the finite incubation time was clearly observed. Especially, the incubation time under the partially amorphized condition was 7 or 17 ns, in reasonable agreements with experiments. However, the significant fluctuation in the incubation time implies that the present simulation is still limited by the finite size and a much larger simulation cell, probably one that is comparable to actual amorphous regions in PCM cells including about 100,000 atoms, is needed for a systematic analysis on the temperature-dependent incubation time. This would be a subject in future study. In conclusion, by suggesting an efficient method to develop NNPs addressing the medium-range order, this work will contribute to simulating phase change materials more accurately and realistically.

CRediT authorship contribution statement

Dongheon Lee: Data curation, Formal analysis, Writing - original draft. **Kyeongpung Lee:** Data curation, Formal analysis, Writing - review & editing. **Dongsun Yoo:** Writing - review & editing. **Wonseok Jeong:** Writing - review & editing. **Seungwu Han:** Supervision, Writing - review & editing.

Declaration of Competing Interest

The authors declare that they have no known competing financial interests or personal relationships that could have appeared to influence the work reported in this paper.

Acknowledgments

Appendix A. Supplementary data

Supplementary data to this article can be found online at https://doi.org/10.1016/j.commatsci.2020.109725.

References

[1] V. Weidenhof, I. Friedrich, S. Ziegler, M. Wuttig, Laser induced crystallization of amorphous $Ge_2Sb_2Te_5$ films, J. Appl. Phys. 89 (2001) 3168.

[2] F. Xiong, A.D. Liao, D. Estrada, E. Pop, Low-power switching of phase-change materials with carbon nanotube electrodes, Science 332 (2011) 568.

[3] S. Song, Z. Song, L. Wu, B. Liu, S. Feng, Stress reduction and performance improvement of phase change memory cell by using $Ge_2Sb_2Te_5$–TaO_x composite films, J. Appl. Phys. 109 (2011) 034503.

[4] B. Gleixner, A. Pirovano, J. Sarkar, F. Ottogalli, E. Tortorelli, M. Tosi, R. Bez, Data retention characterization of phase-change memory arrays, Proc. IEEE Int. Reliab. Phys. Symp. 45 (2007) 542.

[5] Intel Corporation, Intel® Optane™ Technology. URL: https://www.intel.com/content/www/us/en/architecture-and-technology/intel-optane-technology.html (accessed Jan 9, 2020).

[6] J. Tominaga, Topological memory using phase-change materials, MRS Bull. 43 (2018) 347–351.

[7] J. Choe, Intel 3D XPoint memory die removed from Intel Optane™ PCM (Phase Change Memory), Tech Insights, 2017. URL: https://www.techinsights.com/ko/node/16546 (accessed Jan 9, 2020).

[8] F.T. Hady, A. Foong, B. Veal, D. Williams, Platform storage performance with 3D XPoint technology, Proc. IEEE. 105 (2017) 1822–1833.

[9] G.W. Burr, R.M. Shelby, A. Sebastian, S. Kim, S. Kim, S. Sidler, K. Virwani, M. Ishii, P. Narayanan, A. Fumarola, L.L. Sanches, I. Boybat, M. Le Gallo, K. Moon, J. Woo, H. Hwang, Y. Leblebici, Neuromorphic computing using non-volatile memory, Adv. Phys. X. 2 (2017) 89–124.

[10] J. Hegedüs, S.R. Elliott, Microscopic origin of the fast crystallization ability of Ge–Sb–Te phase-change memory materials, Nat. Mater. 7 (2008) 399–405.

[11] J.M. Skelton, A.R. Pallipurath, T.H. Lee, S.R. Elliott, Atomistic origin of the enhanced crystallization speed and n-type conductivity in Bi-doped Ge-Sb-Te phase-change materials, Adv. Funct. Mater. 24 (2014) 7291–7300.

[12] T.H. Lee, D. Loke, S.R. Elliott, Microscopic mechanism of doping-induced kinetically constrained crystallization in phase-change materials, Adv. Mater. 27 (2015) 5477–5483.

[13] J. Behler, First principles neural network potentials for reactive simulations of large molecular and condensed systems, Angew. Chem., Int. Ed. 56 (2017) 12828–12840.

[14] J. Behler, Neural network potential-energy surfaces in chemistry: A tool for large-scale simulations, Phys. Chem. Chem. Phys. 13 (2011) 17930–17955.

[15] Albert P. Bartók, Mike C. Payne, Risi Kondor, Gábor Csányi, Gaussian approximation potentials: The accuracy of quantum mechanics, without the electrons, Phys. Rev. Lett. 104 (2010) 136403.

[16] G.C. Sosso, G. Miceli, S. Caravati, J. Behler, M. Bernasconi, Neural network interatomic potential for the phase change material GeTe, Phys. Rev. B 85 (2012) 174103.

[17] G.C. Sosso, G. Miceli, S. Caravati, F. Giberti, J. Behler, M. Bernasconi, Fast crystallization of the phase change compound GeTe by large-scale molecular dynamics simulations, J. Phys. Chem. Lett. 4 (2013) 4241–4246.

[18] G.C. Sosso, M. Salvalaglio, J. Behler, M. Bernasconi, M. Parrinello, Heterogeneous crystallization of the phase change material GeTe via atomistic simulations, J. Phys. Chem. C. 119 (2015) 6428–6434.

[19] G.C. Sosso, J. Behler, M. Bernasconi, Breakdown of Stokes-Einstein relation in the supercooled liquid state of phase change materials, Phys. Status Solidi B 249 (2012) 1880–1885.

[20] G.C. Sosso, J. Colombo, J. Behler, E. Del Gado, M. Bernasconi, Dynamical heterogeneity in the supercooled liquid state of the phase change material GeTe, J. Phys. Chem. B. 118 (2014) 13621–13628.

[21] S. Gabardi, E. Baldi, E. Bosoni, D. Campi, S. Caravati, G.C. Sosso, J. Behler, M. Bernasconi, Atomistic simulations of the crystallization and aging of GeTe nanowires, J. Phys. Chem. C 121 (2017) 23827–23838.

[22] S. Gabardi, G.G. Sosso, J. Behler, M. Bernasconi, Priming effects in the crystallization of the phase change compound GeTe from atomistic simulations, Faraday Discuss. 213 (2019) 290.

[23] T.H. Lee, S.R. Elliott, *Ab initio* computer simulation of the early stages of crystallization: Application to $Ge_2Sb_2Te_5$ phase-change materials, Phys. Rev. Lett. 107 (2011) 145702.

[24] J. Akola, R.O. Jones, Structural phase transitions on the nanoscale: The crucial pattern in the phase-change materials $Ge_2Sb_2Te_5$ and GeTe, Phys. Rev. B 76 (2007) 235201.

[25] J. Kalikka, J. Akola, R.O. Jones, Crystallization processes in the phase change material $Ge_2Sb_2Te_5$: Unbiased density functional/molecular dynamics simulations, Phys. Rev. B 94 (2016) 134105.

[26] J. Im, E. Cho, D. Kim, H. Horii, J. Ihm, S. Han, Effects of pressure on atomic and electronic structure and crystallization dynamics of amorphous $Ge_2Sb_2Te_5$, Phys. Rev. B 81 (2010) 245211.

[27] S. Kohara, K. Kato, S. Kimura, H. Tanaka, T. Usuki, K. Suzuya, H. Tanaka, Y. Moritomo, T. Matsunaga, N. Yamada, Y. Tanaka, H. Suematsu, M. Takata, Structural basis for the fast phase change of $Ge_2Sb_2Te_5$: Ring statistics analogy between the crystal and amorphous states, Appl. Phys. Lett. 89 (2006) 201910.

[28] D. Loke, T.H. Lee, W.J. Wang, L.P. Shi, R. Zhao, Y.C. Yeo, T.C. Chong, S.R. Elliott, Breaking the speed limits of phase-change memory, Science 336 (2012) 1566.

[29] J. Kalikka, J. Akola, J. Larrucea, R.O. Jones, Nucleus-driven crystallization of amorphous $Ge_2Sb_2Te_5$: A density functional study, Phys. Rev. B 86 (2012) 144113.

[30] M. Chen, K.A. Rubin, R.W. Barton, Compound materials for reversible, phase-change optical data storage, Appl. Phys. Lett. 49 (1986) 502–504.

[31] S. Raoux, H.Y. Cheng, M.A. Caldwell, H.S.P. Wong, Crystallization times of Ge-Te phase change materials as a function of composition, Appl. Phys. Lett. 95 (2009) 071910.

[32] W.J. Wang, L.P. Shi, R. Zhao, K.G. Lim, H.K. Lee, T.C. Chong, Y.H. Wu, Fast phase transitions induced by picosecond electrical pulses on phase change memory cells, Appl. Phys. Lett. 93 (2008) 043121.

[33] Y. Zhu, Z. Zhang, S. Song, H. Xie, Z. Song, X. Li, L. Shen, L. Li, L. Wu, B. Liu, Ni-doped GST materials for high speed phase change memory applications, Mater. Res. Bull. 64 (2015) 333.

[34] S. Song, D. Yao, Z. Song, L. Gao, Z. Zhang, L. Li, L. Shen, L. Wu, B. Liu, Y. Cheng, S. Feng, Phase-change properties of GeSbTe thin films deposited by plasma-enchanced atomic layer depositon, Nanoscale Res. Lett. 10 (2015) 89.

[35] Y. Chen, G. Wang, L. Song, X. Shen, J. Wang, J. Huo, R. Wang, T. Xu, S. Dai, Q. Nie, Unraveling the crystallization kinetics of supercooled liquid GeTe by ultrafast calorimetry, Cryst. Growth Des. 17 (2017) 3687–3693.

[36] G. Bruns, P. Merkelbach, C. Schlockermann, M. Salinga, M. Wuttig, T.D. Happ, J.B. Philipp, M. Kund, Nanosecond switching in GeTe phase change memory cells, Appl. Phys. Lett. 95 (2009) 043108.

[37] G. Kresse, J. Hafner, *Ab initio* molecular dynamics for liquid metals, Phys. Rev. B 47 (1993) 558–561.

[38] P.E. Blöchl, Projector augmented-wave method, Phys. Rev. B 50 (1994) 17953–17979.

[39] J.P. Perdew, K. Burke, M. Ernzerhof, Generalized gradient approximation made simple, Phys. Rev. Lett. 77 (1996) 3865–3868.

[40] D. Yoo, K. Lee, W. Jeong, D. Lee, S. Watanabe, S. Han, Atomic energy mapping of neural network potential, Phys. Rev. Mater. 3 (2019) 093802.

[41] K. Lee, D. Yoo, W. Jeong, S. Han, SIMPLE-NN: An efficient package for training and executing neural-network interatomic potentials, Comput. Phys. Commun. 242 (2019) 95–103 (https://github.com/MDIL-SNU/SIMPLE-NN).

[42] J. Behler, Atom-centered symmetry functions for constructing high-dimensional neural network potentials, J. Chem. Phys. 134 (2011) 074106.

[43] N. Artrith, A. Urban, An implementation of artificial neural-network potentials for atomistic materials simulations: Performance for TiO_2, Comput. Mater. Sci. 114 (2016) 135–150.

[44] S. Plimpton, Fast parallel algorithms for short-range molecular dynamics, J. Comput. Phys. 117 (1995) 1–19.

[45] D. Lee, G. Kang, K. Lee, S. Yoon, J. Kim, S. Han, First-principles calculations on effects of Al and Ga dopants on atomic and electronic structures of amorphous $Ge_2Sb_2Te_5$, J. Appl. Phys. 125 (2019) 035701.

[46] A. Velea, F. Sava, G. Socol, A.M. Vlaicu, C. Mihai, A. Lőrinczi, I.D. Simandan, Thermal stability of phase change GaSb\GeTe, SnSe\GeTe and GaSb\SnSe double stacked films revealed by X-ray reflectometry and X-ray diffraction, J. Non-Cryst. Solids 492 (2018) 11–17.

[47] J.P. McHuglz, W.A. Tiller, The germanium-tellurium phase diagram in the vicinity of the compound GeTe, Trans. Metall. Soc. AIME. 218 (1960) 187.

[48] Yimin Chen, Mu. Sen, Guoxiang Wang, Xiang Shen, Junqiang Wang, Shixun Dai, Xu. Tiefeng, Qiuhua Nie, Rongping Wang, Resolving glass transition in Te-based phase-change materials by modulated differential scanning calorimetry, Appl. Phys. Express 10 (2017) 105601.

[49] J. Im, E. Cho, D. Kim, H. Horii, J. Ihm, S. Han, A microscopic model for resistance

drift in amorphous $Ge_2Sb_2Te_5$, Curr. Appl. Phys. 11 (2011) e82–e84.

[50] P.J. Steinhardt, D.R. Nelson, M. Ronchetti, Bond-orientational order in liquids and glasses, Phys. Rev. B. 28 (1983) 784–805.

[51] S. Raoux, W. Wełnic, D. Ielmini, Phase change materials and their application to nonvolatile memories, Chem. Rev. 110 (2010) 240–267.

[52] W. Jeong, K. Lee, D. Yoo, D. Lee, S. Han, Toward reliable and transferable machine learning potentials: Uniform training by overcoming sampling bias, J. Phys. Chem. C. 122 (2018) 22790–22795.

[53] S. Le Roux, P. Jund, Ring statistics analysis of topological networks: New approach and application to amorphous GeS_2 and SiO_2 systems, Comput. Mater. Sci. 49

(2010) 70–83.

[54] R. Hashimoto, Y. Shibuta, T. Suzuki, Estimation of solid-liquid interfacial energy from Gibbs-Thomson effect: A molecular dynamics study, ISIJ Int. 51 (2011) 1664–1667.

[55] J. Orava, A.L. Greer, Classical-nucleation-theory analysis of priming in chalcogenide phase-change memory, Acta Mater. 139 (2017) 226–235.

[56] F. Spaepen, R.B. Meyer, The surface tension in a structural model for the solid-liquid interface, Scripta Metall. 10 (1976) 257–263.

[57] A.V. Kolobv, J. Tominaga, P. Fons, T. Uruga, Local structure of crystallized GeTe films, Appl. Phys. Lett. 82 (2003) 382.